Determining the angles of squat cracks via CT scanning and metallographic observations

Naeimi, Meysam; Li, Zili; Dollevoet, Rolf

DOI
10.1016/j.engfracmech.2020.107016

Publication date
2020

Document Version
Final published version

Published in
Engineering Fracture Mechanics

Engineering Fracture Mechanics 230 (2020) 107016

Contents lists available at ScienceDirect

Engineering Fracture Mechanics

journal homepage: www.elsevier.com/locate/engfracmech

Determining the angles of squat cracks via CT scanning and metallographic observations

Meysam Naeimi, Zili Li*, Rolf Dollevoet

Section of Railway Engineering, Faculty of Civil Engineering and Geoscience, Delft University of Technology, Delft, the Netherlands

ARTICLE INFO

Keywords:
Squat
Primary crack
Secondary crack
Crack angle
Crack orientation
CT scan
Serial cutting

ABSTRACT

This study investigates the angles θ_1, θ_2, and θ_3 that squat crack faces form with respect to three orthogonal planes: the rail top, the longitudinal-vertical cross-section and the lateral-vertical cross-section. Rail samples with squats of various severities are obtained from the field. Their three-dimensional crack networks are reconstructed using CT (computed tomography) scanning and serial cutting. A 3D visualization method, together with the necessary geometric definitions, is developed for enabling effective measurement and characterization of the squat cracks. It is found that the cracks can be characterized by four orientations (T1 – T4). The variation ranges of the crack angles are determined for each orientation that satisfies $132^\circ \leq \theta_1 \leq 150^\circ$, $6^\circ \leq \theta_2 \leq 36^\circ$ and $67^\circ \leq \theta_3 \leq 81^\circ$. By investigating the occurrence frequency of the orientations, it is found that T4 and T1 together form the primary V-shaped cracks of the squats, and T2 and T3 together form the secondary V-shaped cracks. A finite element modelling of the wheel-track system, in combination with contact mechanics and multi-axial fatigue analysis, successfully relates the stress state to the RCF cracks.

1. Introduction

Squats are a type of rolling contact fatigue (RCF) that occurs in the railhead, and they can develop into rail fractures if they are not detected and treated effectively via maintenance measures. Squats occur mostly in the running band of rails and can create high dynamic forces. These defects are prevalent RCF defects in the Netherlands. They are often found in tangent tracks or shallow curves mostly in the form of isolated dark depressions in the railhead. They often have a two-lung shape appearance in their mature phase [1].

The severity of squats can be identified from their visual appearance in the rail surface as being light, moderate and severe [1]; the classification is explained in Section 2. Apart from dark depression, squat defects typically appear along with cracks in the rail surface and subsurface. In the present research, we consider the geometry of defect (dark depression and plastic deformation) as the “squat defect” or squat in short. The entire crack network (in the rail surface and subsurface) is considered as “cracks within squat” or squat cracks in short.

After initiation, squat cracks continue to grow. Researchers have studied the development process of squats when cracks were already present; see, e.g., [2,3]. Squat cracks are numerically modeled in [2] to study the state of stress intensity factors in the vicinity of the crack front. A modeling approach is proposed in [3] for investigating the crack growth process. Both consider a plane oblique crack in the railhead and investigate its further development. Another example of the use of this approach can be found in [4].

Among the various stages of the squat crack evolution, the initiation phase is crucial. Researchers [5,6] explained the fatigue

* Corresponding author.
E-mail address: Z.Li@tudelft.nl (Z. Li).

https://doi.org/10.1016/j.engfracmech.2020.107016
Received 16 October 2019; Received in revised form 16 March 2020; Accepted 19 March 2020
Available online 27 March 2020

initiation process using the microstructural features that are observed within squats. The early life of a rail squat is studied in [5], where three stages of crack formation have been identified for typical squats. They found that the early stage of crack initiation is due to ratcheting or to the formation of the white etching layer (WEL). According to a recent study [7], thermal effects could cause WEL formation and lower the shakedown limits. Metallurgical investigations were conducted on rails with squats in [6], where the influence of the microstructure was found to be crucial for the formation of squats.

Researchers [7–10] proposed numerical methods for estimating the stress–strain levels inside rails and for predicting the RCF initiation based on the finite element method (FEM) and contact mechanics. The material ratchetting response was found to be an initiation mechanism for RCF defects [8].

Squats typically have a complex crack network below the rail surface, especially when they are highly developed. The terms that are related to the crack geometry will be defined in Section 2.1. Among the various crack planes in a squat crack network, the crack planes that intersect the rail surface can potentially be the initiating cracks. Such crack planes must be studied to investigate the initiation phenomena that are behind the occurrence of squat defects.

The angles for the initiation of RCF cracks were calculated in [8] using the results from FEM simulations. Numerical predictions on crack angles for general RCF cracks can be found in [11,12]. However, these references are not dedicated to rail squats but to crack initiation within the gauge corner contact, where head checks are more prevalent. Next to the experimental observations in the current research, a finite element model of the wheel-track system is employed for numerical calculation of the RCF crack angles.

A recent study [13] has investigated the formation of rail squats using five-year continual field monitoring data on many squats. Various stages of the complete life cycle of squats that were accompanied by cracks were analyzed [13]. This analysis provides statistic observations of the locations and the angles of crack initiation of squats.

The visual appearance of squats varies from a single dark spot up to a complete two-lung shape footprint on the rail surface depending on the severity. Note that light and baby squats (the classification is explained in Section 2) are sometimes difficult or even impossible to be identified by naked eyes. In the present study, we studied the subsurface state of squats (invisible part) using the proposed measurement techniques. This is possible by characterising the geometry of cracks that are associated with the squats.

The 3D geometry of the squat cracks under the rail surface has not been systematically investigated in the literature. Insufficient research has been conducted on measuring the crack angles of the squats via advanced methods such as metallography and computed tomography (CT). The present study seeks to remedy this lack of knowledge by offering metallographic and tomographic observations on squat defects of various severities.

Five rail samples with squat defects of various severities are obtained from the Dutch railway network and subjected to CT scanning and metallographic inspections. The 3D geometries of the subsurface squat crack networks are determined. Using these data, the crack angles are defined and measured. Afterwards, a categorization is proposed for the studied cracks and the characteristic ranges of the angles are determined for each category. The crack angles are also predicted by numerical simulations using a 3D model of the wheel-track system.

2. Measuring squat crack angles that are formed at the rail surface

A straight track between Meppel and Leeuwarden in the Dutch railway network is selected for sampling the squats. The rail was manufactured in 1989 and was loaded with an annual gross tonnage of approximately 3.65 million tons [14]. Five rail samples that contain squats are obtained from various places along this track. Table 1 presents an overview of the studied defects and their classifications according to severity. The defects are classified into A and B (light and moderate squats) according to [1]. Severe squats (see Fig. 1(c) of [1] for example) are not analyzed in the present study as their crack network are too complicated and not necessarily characteristic of squats anymore.

Two moderate squats and one light squat are studied; see Table 1. The term “baby squat” is suggested in [16]. The last defect (Sample-5) is smaller than a baby squat and does not fall into any category that was proposed by [1] or [16]. In this study, we use the term ‘initiating RCF crack’ for this type of defect as it is not certain whether this crack can grow to become a squat. Sample-1, Sample-3 and Sample-4 were used in [16] to demonstrate the CT scanning technique and Sample 3 was used in Fig. 8(b) of [13] to show the 3D crack face of the peninsula.

According to Table 1, two techniques are used for the reconstruction of the crack networks: serial cutting and CT scanning. They are briefly described as follows. Serial cutting (or multisectioning) is a destructive metallographic method that can be used to reconstruct the geometry of subsurface cracks in defected rails. This method was used to inspect RCF cracks in [17], in which 3D data on crack shapes and characteristics were generated. Serial cutting involves the following steps: *(i)* a rail sample is sectioned in

Table 1
Overview of the selected samples and the crack reconstruction techniques.

Sample	Internal TU Delft ID of the sample	Severity of squat/defect	Relevant figure	Reconstruction technique
Sample-1	TU-19	Moderate squat-Class B	Fig. 2	CT Scanning
Sample-2	TU-17	Moderate squat-Class B	Fig. 3	Serial cutting
Sample-3	TU-19	Light squat-Class A	Fig. 4	CT Scanning
Sample-4	TU-10	Baby squat	Fig. 5	CT Scanning
Sample-5	TU-10	Initiating RCF crack (potential squat)	Fig. 6	CT Scanning-Serial cutting

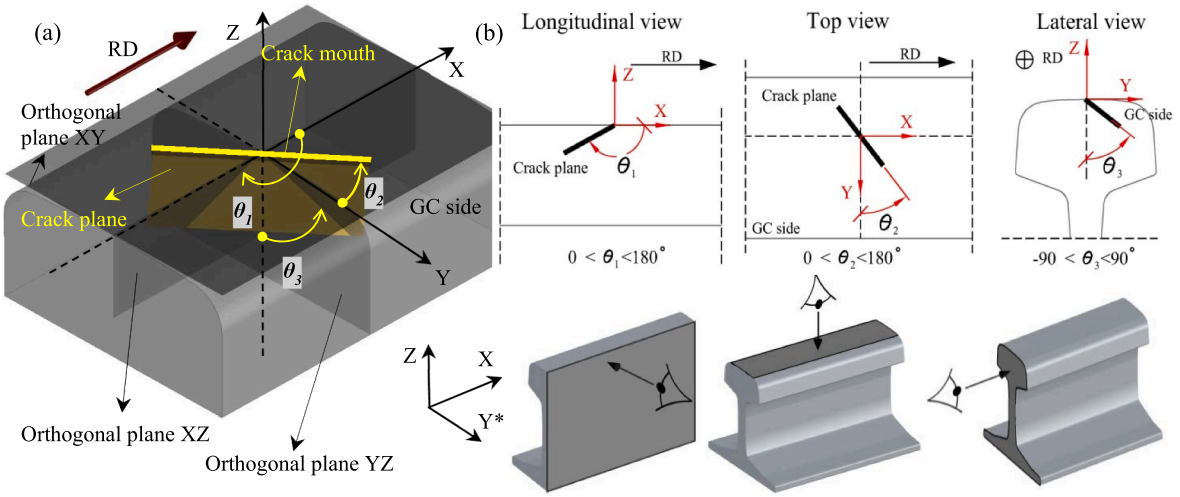

Fig. 1. Schematic view of a squat crack plane and its intersections with the orthogonal planes: (a) A 3D view of the crack plane in the railhead, which shows the angles that are formed in the three orthogonal planes, namely, XY, XZ, and YZ; (b) The intersections of the crack planes with the three orthogonal planes at crack angles θ_1, θ_2, and θ_3; the corresponding view of each orthogonal plane is shown in the lower part of (b)). The viewing directions are marked with eye icons in (b). * Y is the lateral axis toward the gauge corner; hence, the XYZ coordinate system is not necessarily right-handed.

sequential slices by cutting; *(ii)* each section is recorded via optical microscopy (metallographic observation); and *(iii)* 2D cracks at separate sections are aligned and the final 3D volume is reconstructed.

CT is a nondestructive inspection tool that can produce a 3D visualization of an object, including its internal defects. This technique was recently used in [16] for the reconstruction of rail RCF defects. The CT scanning technique involves the following steps: *(i)* a rail sample is prepared and inserted into the CT scanner; *(ii)* X-ray images are captured of the object at various angles during the CT scan; *(iii)* the cross-sectional (tomographic) images are combined to form 3D volumetric data of the object, including its internal fractures; *(iv)* the tomographic data are further processed by using the image processing tools to detect all the surface and subsurface cracks in the bulk steel; and *(v)* the 3D geometry of the internal crack networks is reconstructed and is made available for quantification and visualization.

A Phoenix Nanotom™ micro CT scanner is used in the present research. Rail samples are laid and glued on an object platform before being inserted into the CT scanner. The X-rays are generated at 180 kV, and the maximum spatial resolution (minimum voxel size) is 300 nm. Such a high resolution is the maximum nominal capability of the CT device; the actual resolution is dependent on the type of materials to be studied, sample size, radiation power and storage capacities. A voxel size of 12 μm × 12 μm × 12 μm was used to study RCF cracks in the rail steel in the present research considering the size of the prepared specimens. The highest detectability of the facility is down to 200 nm. The object platform is located between the X-ray source and data acquisition screen [16]. More details of the measurement process and the subsequent data postprocessing are presented in [16]. By choosing the appropriate settings and specimen size, CT can accurately reconstruct the squat cracks at different growth stages. By using the procedure and the recommendations described in [16], researchers will be able to use CT as a reliable tool for the non-destructive reconstruction of squat crack networks and for the measurement of the crack geometries.

Both techniques can produce 3D geometries of the internal crack networks in squats. However, CT is used more frequently in this study due to the advantages that are described in [16], among them that the sample can be saved for further microstructural examinations after the nondestructive CT scanning. [16] has reported the development process of CT-technology for the rail application. Contrary to [16], we have used the results of the CT-technique in the present study for quantification purposes and calculation of the crack angles.

2.1. Definitions and conventions on the crack plane and crack angles

A 3D coordinate system (X, Y, Z) is introduced with

- X pointing in the rolling direction of the train wheels;
- Y pointing to the gauge side. Note: the left and right rails of the track have opposite Y-axes; hence, the XYZ coordinate system is not necessarily right-handed;
- Z pointing vertically and upward.

Fig. 1 shows a schematic view of a squat crack and its intersection with the rail surface. Hereby, we define several terms regarding

the crack geometry for characterizing and measuring the crack:

- Orthogonal planes: The three planes, namely, YZ, ZX, and XY (lateral-vertical, longitudinal-vertical and horizontal);
- Crack network: The entire 3D geometry of the crack. It may contain one or more crack faces;
- Crack mouth: The crack in the rail top view when the crack face is viewed at its intersection with the rail surface;
- Crack trajectory: The intersection of the crack face with the orthogonal planes;
- Crack face unit: A crack face is divided into several areas. Each such area is a crack face unit;
- Crack plane: The plane that is tangent to a crack face unit, denoted Ci (i = 1, … 7);
- Crack angles θ_1, θ_2, and θ_3: The three angles at which the crack plane intersects with the three orthogonal planes, see Fig. 1;
- Crack orientations: Four special categories of crack planes that can be identified when examining the orientation of the crack plane relative to the orthogonal planes; see Section 4.1.

Based on these definitions, we will be able to characterize the geometries of complex cracks. Fig. 1(a) shows an oblique crack plane in the (X, Y, Z) coordinate system. The gauge corner side and the rolling direction of the train wheel are labeled as the GC side and RD, respectively. This oblique crack intersects the orthogonal planes with the angles θ_1, θ_2, and θ_3; see Fig. 1(b).

A squat crack in the very beginning stage of development can already have a curved surface, as observed in [13]. For the measurement and characterization, such a curved surface is divided into a series of surface units. The crack plane, namely, the plane that is tangent to a surface unit, intersects the orthogonal planes with the angles θ_1, θ_2, and θ_3 as illustrated in Fig. 1. These angles are the angles of the crack plane with respect to the axes X, Y and Z. The variation ranges of these angles are specified in Fig. 1(b).

2.2. Measurement of the crack angles in various samples

The 3D crack networks of the studied squats are reconstructed using serial cutting and CT scanning. The results are presented in this section and the crack angles θ_1, θ_2, and θ_3 are measured.

2.2.1. Sample-1

Details on the sample and the CT scan observations of Sample-1 are presented in Fig. 2. Top views of the defect in the field and in

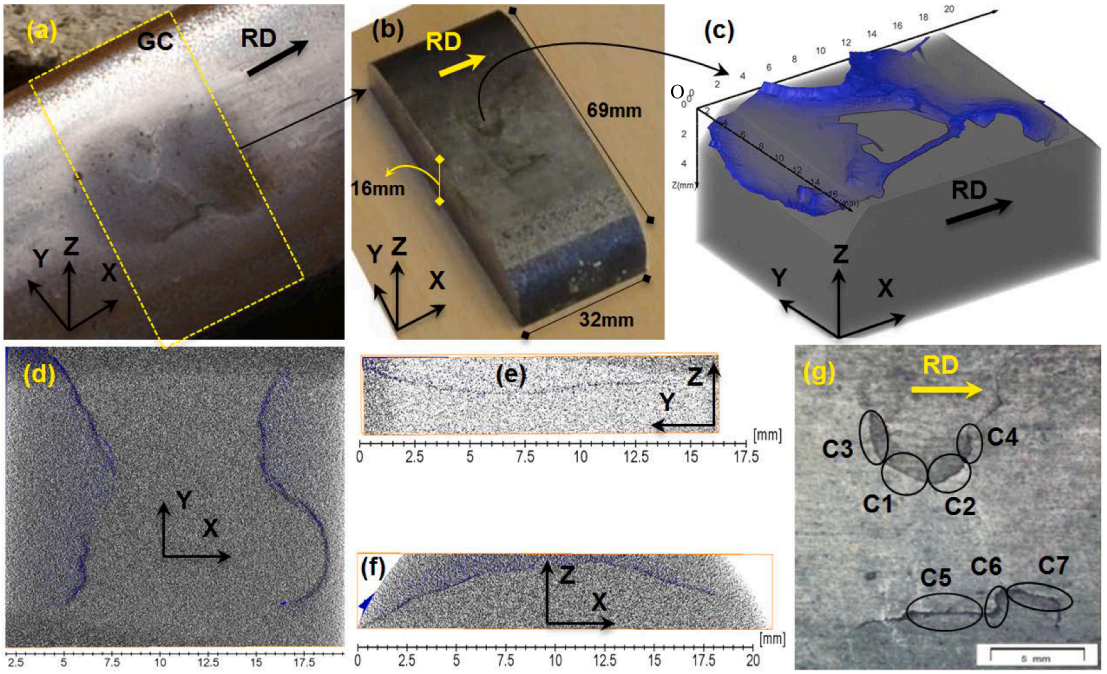

Fig. 2. Details of the sample and the CT scan observations of Sample-1. (a) A top view of the squat when the rail was still in service; (b) the rail sample that was prepared for the CT scan; (c) a 3D visualization of the rail with its internal 3D crack network; (d, e, f) three examples of 2D tomographic images on the orthogonal planes that show the crack trajectories; (d) is a 2D image at approximately 3 mm under the rail surface; (e) is approximately 15 mm away from the origin of the coordinate system O; (f) is approximately 4 mm away from the origin of the coordinate system O, see [16] for details about the location of 2D tomographic images in the rail bulk and (g) the rail surface with the crack mouths divided into seven segments that correspond to seven crack planes (C1-7) that the intersect the rail surface; Ci s (i = 1, … 7) are shown next to the crack mouths because adding 3D crack planes into the existing rail picture is not possible.

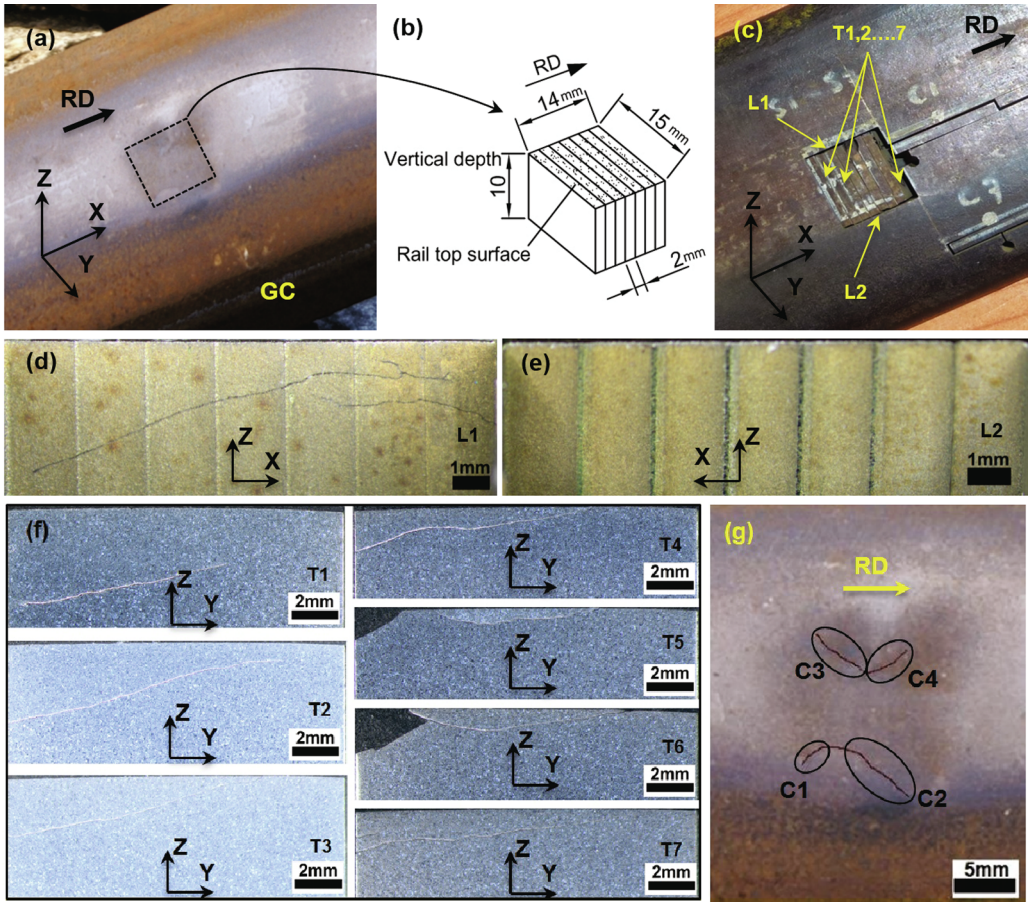

Fig. 3. Details of the sample and the metallographic observations of Sample-2. (a) A top view of the squat when the rail was still in service; (b) the rail cutting pattern and dimensions of the sectioned slices; (c) seven slices after the cutting, lateral sections T1-T7 and longitudinal sections L1 and L2; locations of L1 and L2 are shown in (c); (d, e) metallographic observation of the cracks in the two longitudinal sections, namely, L1 and L2; (f) metallographic observations on the lateral sections, namely, T1-T7, locations of T1-T7 are shown in (c); and (g) the crack segments in the rail surface that correspond to crack planes C1-C4.

the lab are shown in Fig. 2(a) and (b), respectively. Fig. 2(c) shows the 3D crack network of this squat that was reconstructed by CT, in which 50% transparency is applied to the gray bulk steel to highlight the internal crack face. Three examples of 2D tomographic images of the reconstructed rail object are shown in Fig. 2(d, e, f), where the internal cracks are clearly visible in blue color. Fig. 2(g) shows a top view of the rail sample under an optical microscope. As Sample-1 is a moderate squat with the typical two-lung appearance, the cracks have already grown both in the rail surface and in the subsurface. The crack mouths are divided into seven segments C1 – C7. With each segment a unique crack plane can be defined: the intersection of the crack plane with the rail surface is the segment. Thus we use Ci (i = 1, … 7) to denote both a segment and the uniquely associated crack plane, e.g., C1 signifies both segment C1 and crack plane C1. This applies for all the samples.

The crack angles are measured for crack planes C1-C7. The results of the crack angle measurements including the 3D geometry of the internal cracks of all the rail samples are provided in Appendix A. The results of crack angle measurements for all the rail samples are summarized at the end of Section 2.

2.2.2. Sample-2

Sample-2 is examined via serial cutting for reconstructing the internal crack networks. Details of the sample and the metallographic observations are presented in Fig. 3. Fig. 3(a) shows the moderate squat when the rail was still in service. A rectangular block of size 14 × 15 × 10 mm, which consists of seven sequential thin slices, is prepared from the railhead; see Fig. 3(b, c). The direction of cutting is perpendicular to the direction of traffic and the slice thickness is 2 mm. The seven slices are ground and polished for the metallographic observations. Then, the cracks are observed under an optical microscope. The geometry of the cracks in each slice is examined and the crack tip locations, angles, sizes and depth are measured. In addition to the lateral sections (T1-T7), two longitudinal sections (L1, L2) are observed under the microscope. The results of metallographic observations on L1 and L2 are shown in Fig. 3(d, e), and Fig. 3(f) shows the corresponding results on T1-T7. Fig. 3(g) shows the crack segments in the rail surface, where four

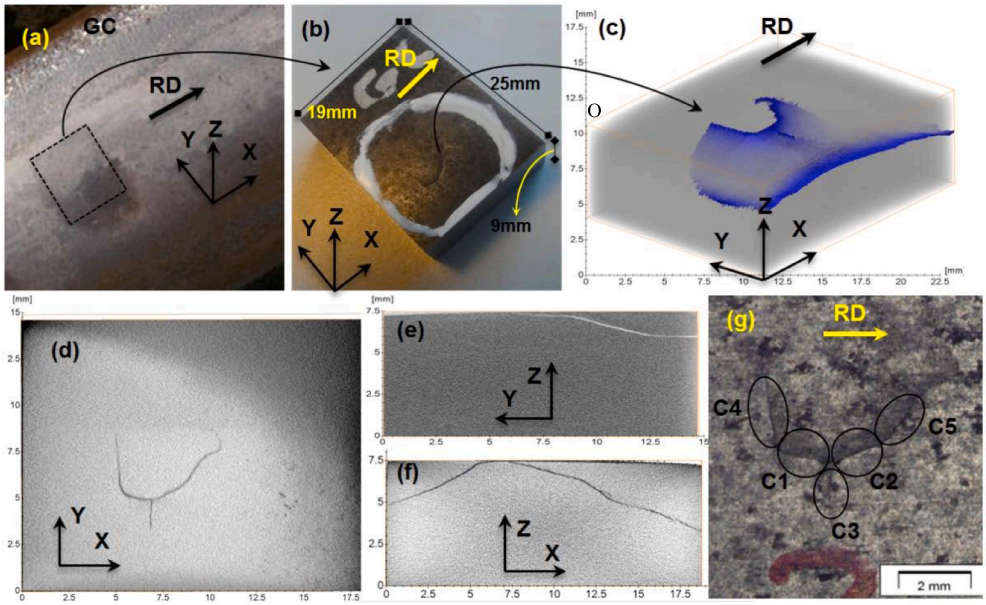

Fig. 4. Details on the sample and the CT scan observations of Sample-3. (a) A top view of the squat when the rail was still in service; (b) the rail sample that was prepared for the CT scan; (c) a 3D visualization of the rail with the internal 3D crack network; (d, e, f) three examples of 2D tomographic images on orthogonal planes that show the crack trajectories; (d) is a 2D image at approximately 1 mm under the rail surface; (e) is approximately 7 mm away from O; (f) is approximately 10 mm away from O, see [16] for details about the location of 2D tomographic images in the rail bulk and (g) a metallographic view of the rail surface with five crack segments as the intersections of the squat crack planes with the rail surface.

crack planes (C1-C4) are defined. The crack trajectories of 2D slices T1-T7, L1, and L2 are combined with interpolation to generate 3D data on the internal crack network.

2.2.3. Sample-3

Details on the sample and the CT scan observations of Sample-3 are presented in Fig. 4. The development process and the shape of this squat are discussed in [13]. Top views of the rail when it was still in the field and the prepared CT sample are shown in Fig. 4(a, b). Fig. 4(c) shows the 3D geometry of the internal crack networks in this squat and examples of 2D topographic images are shown in Fig. 4(d, e, f). For this squat, five crack segments are considered in the rail surface, as shown in Fig. 4(g).

2.2.4. Sample-4

Details on the sample and the CT scan observations are presented in Fig. 5. Fig. 5(a, b) show top views of the rail in the field and the corresponding CT sample. Fig. 5(c) shows the 3D crack network that is reconstructed for this squat and examples of 2D topographic images are shown in Fig. 5(d, e, f). For this squat, four crack segments (C1-C4) are considered in the rail surface, as shown in Fig. 5(g).

2.2.5. Sample-5

The last defect (Sample-5) is not visible to the naked eye; however, we predicted the occurrence of initiating RCF cracks in the chosen area. We suspected that this place could have RCF cracks in an early stage of development since squats and corrugation were found nearby; one of the squats was Sample-4.

A rectangular block is obtained from the railhead next to Sample-4; see Fig. 6(a, b). In the beginning, we inspected a length of approximately 120 mm around Sample-4 under the optical microscope and the choice on the block of Sample-5 (Fig. 6(b)) was made when we were sure of the presence of cracks in the area. Fig. 6(d) shows the sample under an optical microscope with the resolution of 20x. No cracks are visible at this resolution. Performing CT on the sample of Fig. 6(b) also provided no information on the cracks in the bulk steel.

Then, this sample is cut smaller (Fig. 6(c)) to generate CT results of higher resolution; see the discussion on the sample size in [16]. A high-resolution optical microscope (500x) is used to inspect the surface of the new sample. This time, two tiny cracks (size of approximately 80 μm) are found; see Fig. 6(e). These surface cracks are observed in the longitudinal orthogonal plane (XZ), as shown in Fig. 6(f). The CT scan on the new sample provided data on the 3D geometry of these cracks; they are presented in Fig. 6(g, h). Three examples of 2D tomographic images are presented in Fig. 6(g). Fig. 6(h) presents the 3D geometries of these two cracks (C1 and C2). This observation cannot confirm that the tiny cracks in Sample-5 will further develop into a squat, as they might disappear due to, e.g., natural wear or spalling.

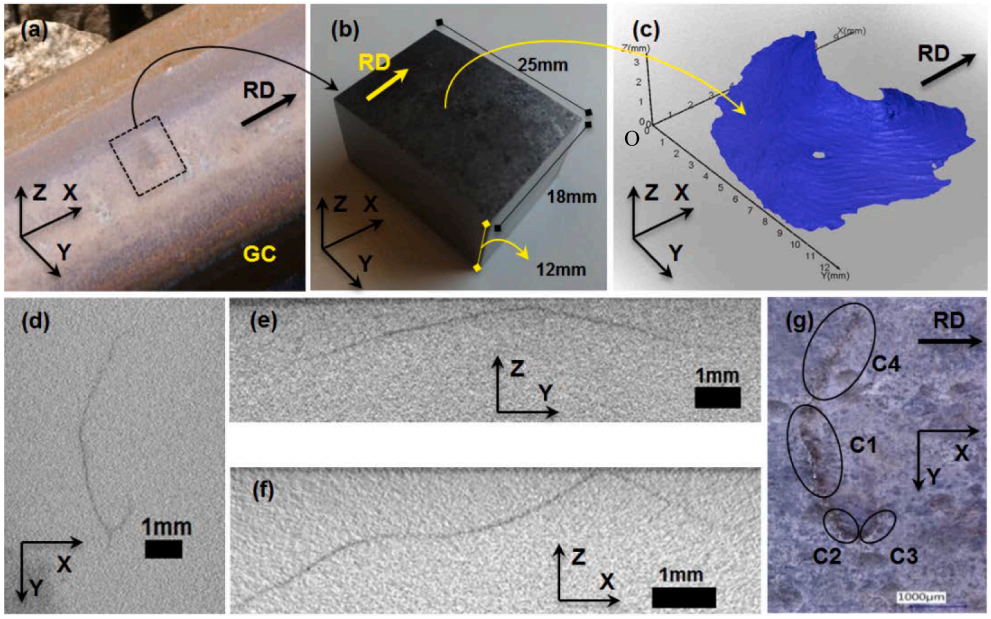

Fig. 5. Details on the sample and the CT scan observations of Sample-4; (a) A top view of the squat defect when the rail was still in service; (b) the rail sample that was prepared for the CT scan; (c) a 3D visualization of the rail with the internal 3D crack surface; (d, e, f) three examples of 2D sections on orthogonal planes that show the crack trajectories; (d) is a 2D image at approximately 0.5 mm under the rail surface; (e) is approximately 9 mm away from O; (f) is approximately 13 mm away from O, see [16] for details about the location of 2D tomographic images in the rail bulk and (g) a metallographic view of the rail surface with four crack segments as the intersections of the crack planes with the rail surface.

Table 2 summarizes the crack angles of the crack planes in all the rail samples. Detailed discussions on the characteristic angle ranges are provided in Section 4.

3. Calculation of crack angles by numerical modelling

The experimental observations made in this research are phenomena related to the fracture mechanical behaviour of the rails in RCF conditions. To understand the observations, a finite element model of the wheel-track system is employed for a preliminary numerical analysis of the RCF angles in an attempt to correlate the stress state to the cracks. The FE model and the crack initiation mechanism (based on the stress states) cannot necessarily distinguish between the types of the RCF (e.g., between squat and head check [22], whose crack angles can be similar); therefore, we use the general term “RCF crack” in the numerical part.

Contact mechanics and multi-axial fatigue analysis are used to study the crack initiation stress state in rails. Various loading conditions are modelled. Employing the critical plane concept [23], the rail elements with the highest potential for crack initiation are determined, based on which, the 3D geometry of the potential RCF cracks are estimated. The results of the crack angles are then presented.

3.1. Finite element modelling

The finite element model of the wheel-track system considers a single wheel running over a length of a straight railway track; see Fig. 7(a). The standard rail profile UIC 54E1 with an inclination of 1:40 at the rail foot is used. By employing an adaptive meshing method, the smallest element size in the wheel-rail contact interface is 0.4 mm. The contact surfaces of both the wheel and rail are smooth. The sprung mass of the vehicle, which together with the unsprung wheel mass form the wheel loads, is lumped and supported by a group of springs and dampers of the primary suspension. The track system is modelled of the typical ballasted railway track, in which, the rail is resting on sleepers with in-between spring/dampers serving as the fasteners. The sleepers are laid on the underlying spring/dampers as the ballast.

A time-domain finite element analysis with the explicit algorithm is employed using the approach described in [15,18]. The parameters of the finite element model are listed in Table 3. The materials in the contact interface are considered elastic–plastic with the properties given in Table 3.

Different values of the traction coefficient (μ) are used to simulate the braking and traction behaviour of the train wheel. The positive value ($\mu = 0.35$) represents the tractive wheel, while the negative ($\mu = -0.35$) simulates braking. The case $\mu = 0$ simulates free rolling contact of the wheel over the rail.

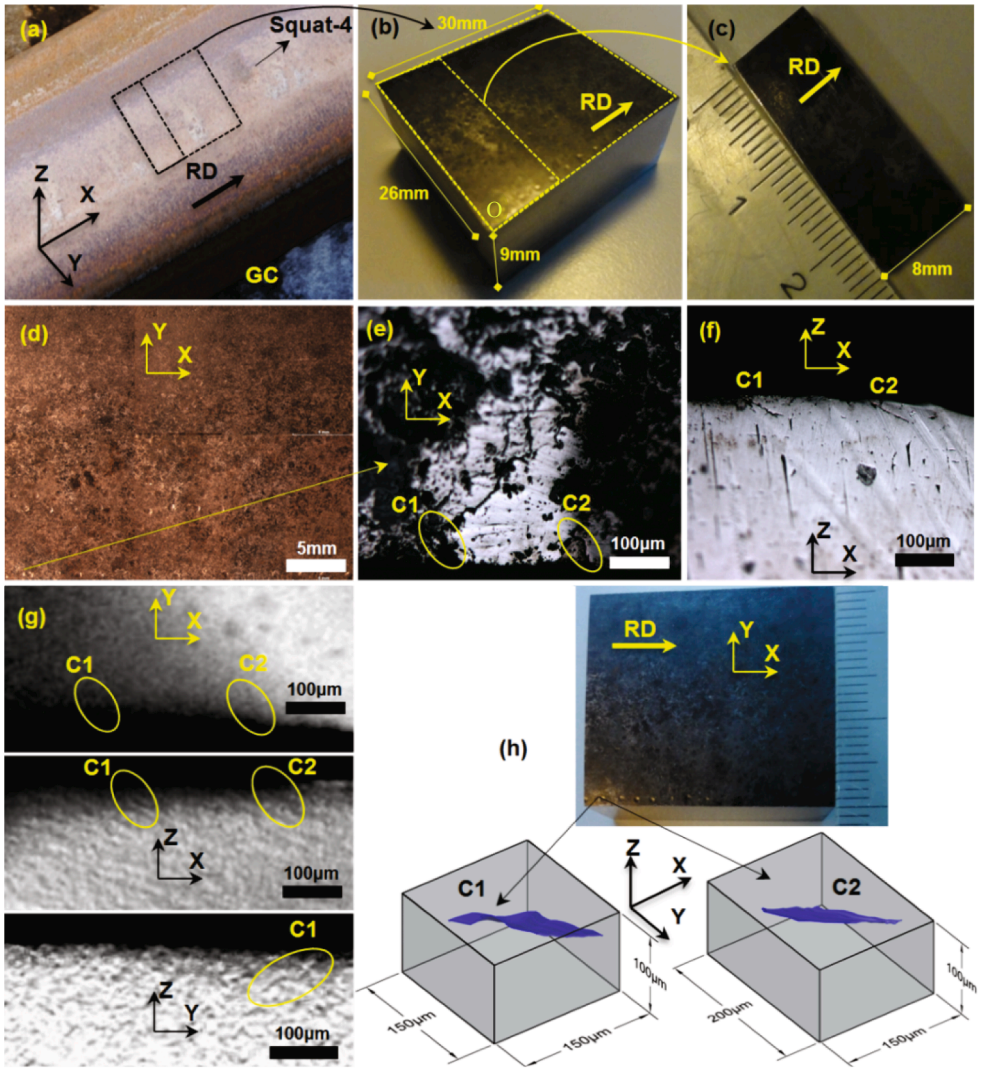

Fig. 6. Reconstruction of the two tiny cracks in Sample-5. (a) A top view of the rail when the rail was still in service; (b, c) two rail samples that were prepared for the CT scan; (d) the large sample of (b) under the microscope at 20x resolution; (e) a microscopic view of the rail sample with two tiny cracks at 500x resolution; (f) the same cracks in the longitudinal orthogonal plane; (g) three examples of the 2D tomographic images from the CT scan; XY image is a 2D image at approximately 0.1 mm under the rail surface; (e) XZ image is approximately 2 mm away from O; YZ image is approximately 2 mm away from O and (h) 3D visualization of the rail with internal cracks C1 and C2.

3.2. Fatigue initiation criteria

Up to now, various fatigue criteria have been employed to quantify fatigue initiation life of materials, mostly by using calculated stresses and strains out of numerical models. Some critical reviews on different predictive models of fatigue crack initiation in engineering materials including metals are provided in [19,20]. Wheels and rails are subjected to a non-proportional multiaxial stress condition, which causes variation in the directions of the principal stresses and the maximum shear stresses. Therefore, a multiaxial fatigue criterion that could consider the non-proportional loading condition is more applicable [21].

In the current research, we used the multiaxial fatigue model proposed by Jiang and Sehitoglu [23] for the fatigue initiation analysis. This fatigue criterion is used for the wheel-rail contact application in [21] and the fatigue predictions by using that have been reported to be in good agreement with the test results and field observations [21]. This criterion has also been used in [24] for predicting fatigue initiation life of the rail under RCF conditions, in which, reasonable correlations with laboratory test data and field observations were seen. The fatigue parameter in this model is expressed by [23]:

$$FP_{\max} = (\langle \sigma^{\max} \rangle \frac{\Delta\varepsilon}{2} + J\Delta\tau\Delta\gamma)_{\max} \tag{1}$$

Table 2
Results of measuring the crack angles for the crack planes that intersect the rail surface per rail sample Sample-1.

Crack plane:	C1	C2	C3	C4	C5	C6	C7
θ_1	171°	13°	155°	17°	174°	93°	16°
θ_2	67°	122°	28°	150°	89°	176°	79°
θ_3	70°	70°	76°	80°	81°	−53°	−56°

Sample-2

Crack plane:	C1	C2	C3	C4
θ_1	167°	14°	168°	13°
θ_2	59°	112°	124°	53°
θ_3	69°	58°	−73°	−73°

Sample-3

Crack plane:	C1	C2	C3	C4	C5
θ_1	141°	12°	71°	132°	28°
θ_2	79°	114°	177°	6°	147°
θ_3	77°	64°	81°	83°	71°

Sample-4

Crack plane:	C1	C2	C3	C4
θ_1	139°	150°	19°	262°
θ_2	10°	36°	127°	155°
θ_3	81°	67°	65°	−73°

Sample-5

Crack plane:	C1	C2
θ_1	17°	23°
θ_2	58°	41°
θ_3	−63°	−69°

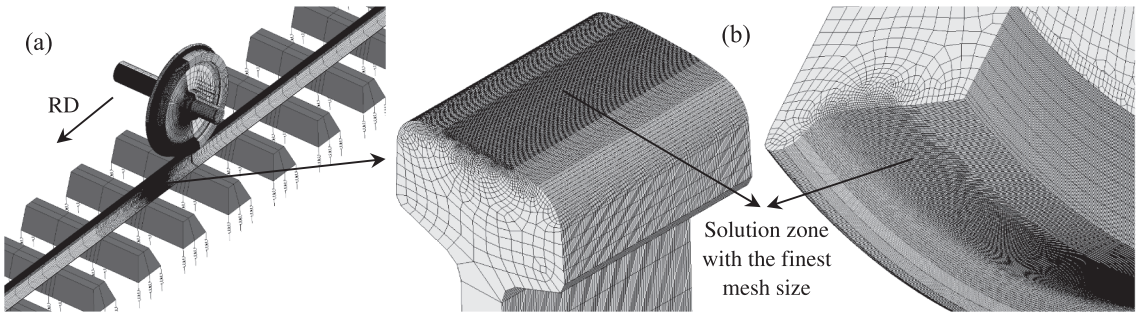

Fig. 7. (a) 3D finite element model of the wheel-track system; (b) magnified view of the rail surface and the wheel tread with the finest mesh arrangement in the solution zone.

where, in each loading cycle, $\Delta\varepsilon$ is the normal strain range, σ_{max} the maximum normal stress, $\Delta\gamma$ the shear strain range, $\Delta\tau$ the shear stress range, J a material-dependent constant and $\langle\,\rangle$ the McCauley bracket $x = (|x| + x)/2$. This model considers the influence of normal and shear loadings on damage occurrence. The first term of this equation considers the mean stress effect in the normal direction, while the second term incorporates the shear stress–strain effects. The stress–strain responses, needed for this equation, are obtained from the finite element analysis.

According to [23], the stress and strain responses in (1) need to be obtained at the critical plane, in which, the largest fatigue parameter (FP_{max}) occurs. The critical plane approach searches for the most potential damage plane, where, a fatigue crack tends to initiate. Any rotation in the global axes, shown in Fig. 1(a), leads to a new fatigue parameter. In this approach, the fatigue parameter is calculated by inspecting all the possible plane orientations by tensor rotations. The crack initiation plane, with angles shown in Fig. 1, corresponds to the orientation which creates the maximum fatigue parameter. The stress components when the coordinate system is subjected to a spatial rotation are shown in Fig. 8 (a, b). As shown in Fig. 8 (c, d) two forms of demonstrations are available

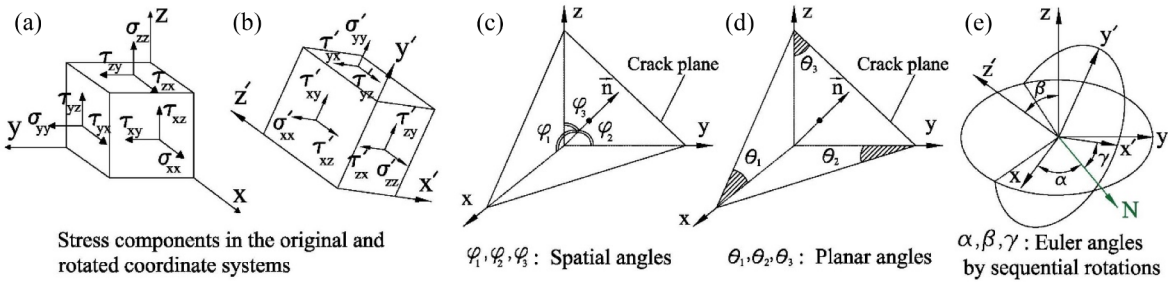

Fig. 8. (a) Stress components of a single element in the original coordinate system; (b) stress components after spatial rotation; (c) spatial angles of the critical plane (crack initiation plane); (d) the corresponding planar angles of the crack plane; (e) Euler angles corresponding to sequential axes rotations.

Table 3
The values of parameters used in the numerical simulations

Parameters (unit)	Values	Parameters (unit)	Values
Static wheel load, M_c (kN)	116.8	Stiffness of primary suspension, K_c (kN/m)	880
Wheel weight, M_w (kg)	900	Damping of primary suspension, C_c (N.s/m)	4000
Wheel diameter (mm)	920	Young's modulus of wheel-rail material, E_r (GPa)	210
Rail weight per length (Kg/m)	54.42	Poisson's ratio of wheel-rail material, ν_r	0.3
Sleeper mass, M_s (kg)	280	Density of wheel-rail material, ρ_r (kg/m^3)	7800
Friction coefficient, f	0.5	Yield stress of the work hardened rail (MPa)	800
Longitudinal traction coefficient, μ_x	−0.35,0, 0.35	Tangent modulus of elastic–plastic rail, E_p (GPa)	21
Rolling speed, V (km/h)	100	Young's modulus of concrete material, E_c (GPa)	38.4
Stiffness of ballast, K_b (kN/m)	45,000	Poisson's ratio of concrete sleeper material, ν_c	0.2
Damping of ballast, C_b (N.s/m)	32,000	Density of sleeper material, ρ_c (kg/m^3)	2520
Stiffness of rail pad, K_p (kN/m)	1,300,000	Constant J in the fatigue criterion	0.2
Damping of rail pad, C_p (N.s/m)	45,000		

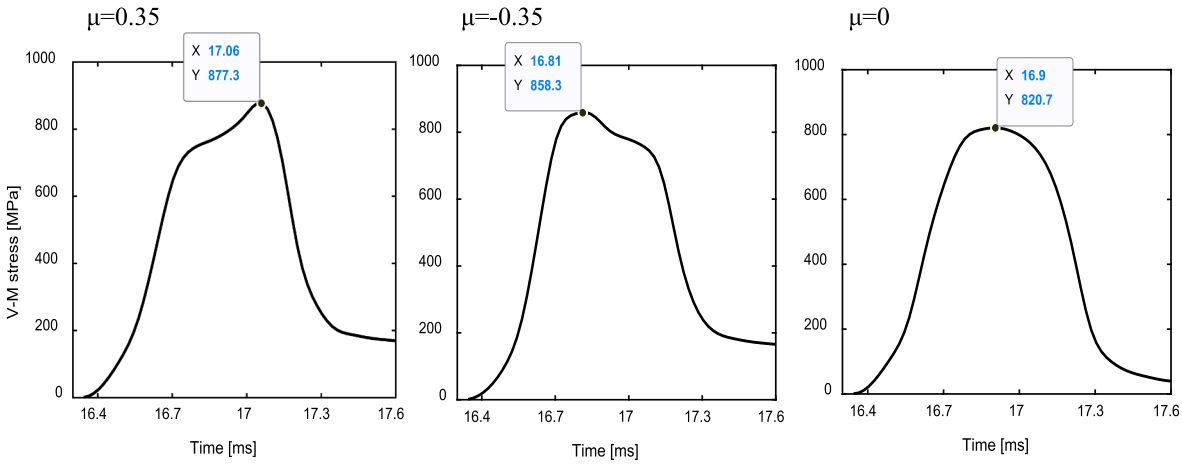

Fig. 9. Time histories of von Mises (V-M) stresses in the rail surface during wheel passage; the results are for different traction coefficients.

for crack plane angles. Fig. 8 (c) shows the spatial angles of the critical plane (φ_1, φ_2, φ_3) with respect to the global axes. Fig. 8 (d) shows the corresponding planar angles (θ_1, θ_2, θ_3), formed by intersection with the orthogonal planes. These 2D planar angles are the same crack angles used for the experimental observations.

The relationship between the spatial angles and the 2D planar angles is written by:

$$\theta_1 = \arctan\left(-\frac{\cos\varphi_3}{\cos\varphi_1}\right),\ \theta_2 = \arctan\left(-\frac{\cos\varphi_1}{\cos\varphi_2}\right),\ \theta_3 = \arctan\left(-\frac{\cos\varphi_2}{\cos\varphi_3}\right) \tag{2}$$

The spatial angles are related to each other by the spherical law of cosines:

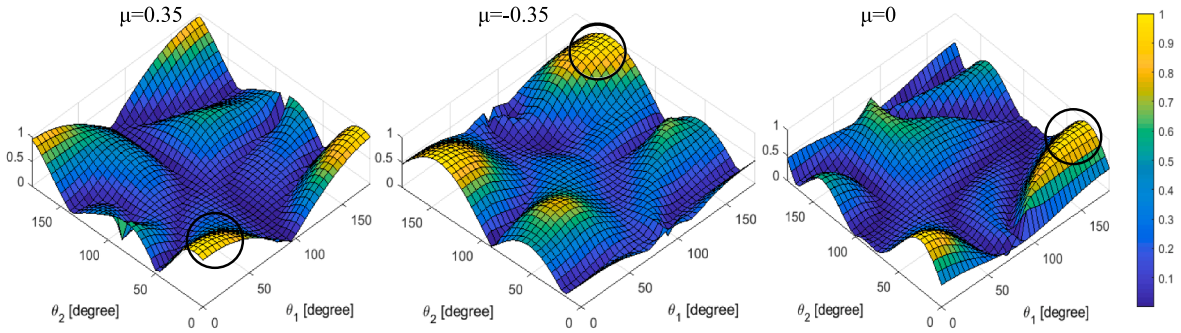

Fig. 10. Searching for the critical plane with the maximum *FP* in the rail element; the higher *FP* (dimensionless) is shown with brighter in yellow and the lower *FP* with darker in blue; the black circles show the regions where the peaks occur. (For interpretation of the references to color in this figure legend, the reader is referred to the web version of this article.)

Table 4
Crack angles calculated by the numerical simulations

Angle	μ = 0.35	μ = −0.35	μ = 0
θ1	19.8	159.9	158.6
θ2	17.6	167.3	36.9
θ3	−83.5	−85.3	73.6

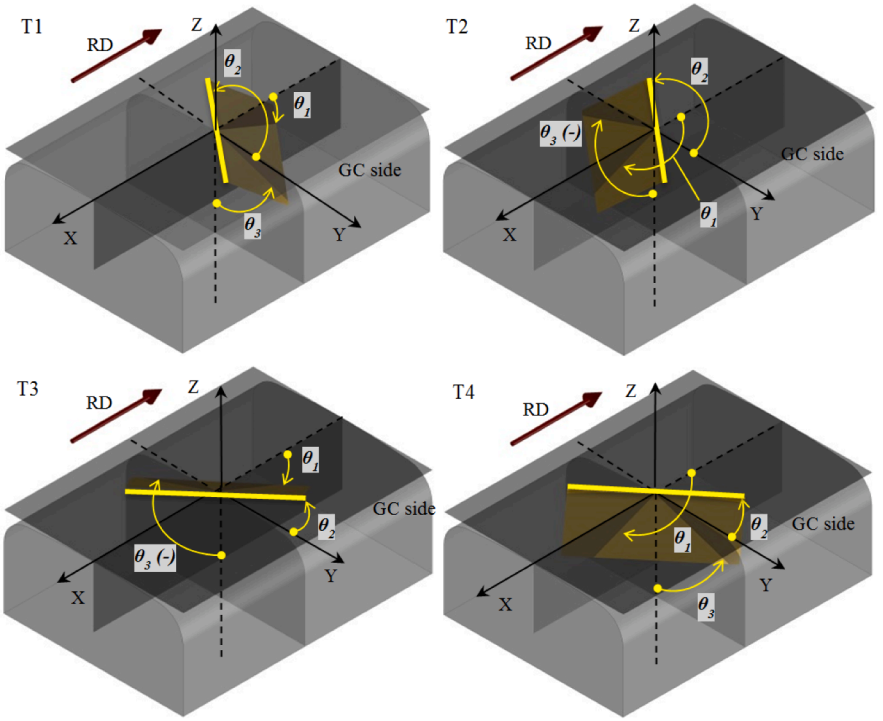

Nominal variation ranges of θ_1, θ_2, and θ_3 for the identified categories:

Orientation category	T1	T2	T3	T4
Angle range θ_1	$0°<\theta_1<90°$	$90°<\theta_1<180°$	$0°<\theta_1<90°$	$90°<\theta_1<180°$
Angle range θ_2	$90°<\theta_2<180°$	$90°<\theta_2<180°$	$0°<\theta_2<90°$	$0°<\theta_2<90°$
Angle range θ_3	$0°<\theta_3<90°$	$-90°<\theta_3<0°$	$-90°<\theta_3<0°$	$0°<\theta_3<90°$

Fig. 11. Four orientations (T1-T4) of the crack planes that intersect the rail surface.

Table 5
Categorization of the crack planes that intersect the rail surface into 4 orientations

Sample-1	Crack plane	C1	C2	C3	C4	C5	C6	C7
	Orientation category	T4	T1	T4	T1	T4	T2	T3
Sample-2	Crack plane	C1	C2	C3	C4			
	Orientation category	T4	T1	T2	T3			
Sample-3	Crack plane	C1	C2	C3	C4	C5		
	Orientation category	T4	T1	T1	T4	T1		
Sample-4	Crack plane	C1	C2	C3	C4			
	Orientation category	T4	T4	T1	T2			
Sample-5	Crack plane	C1	C2					
	Orientation category	T3	T3					

Table 6
Occurrence frequency of each crack orientation category and the variation ranges of θ_1, θ_2, and θ_3

Crack orientation category	T1	T2	T3	T4	Total
Occurrence frequency	6	2	4	8	20
Occurrence percentage	30%	10%	20%	40%	100%
Angle range θ_1	12°–28°	154°–168°	13°–23°	132°–150°	–
Angle range θ_2	112°–150°	124°–155°	41°–79°	6°–36°	–
Angle range θ_3	58°–80°	73°–77° (–)	56°–73° (–)	67°–81°	–

$$\cos^2\varphi_1 + \cos^2\varphi_2 + \cos^2\varphi_3 = 1 \tag{3}$$

and the 2D planner angles are related by:

$$\tan\theta_1 .\ \tan\theta_2 .\ \tan\theta_3 = 1 \tag{4}$$

which means, if two of the 2D angles are known, the third angle can be calculated. The planar angles are calculated in this research, which complies with the experimental observations.

When a Cartesian coordinate system XYZ (the original state, in which the stresses are obtained) is subjected to the transformation, the transformation matrix of the stress tensor is related using:

$$\sigma = \begin{pmatrix} \sigma_x & \tau_{xy} & \tau_{xz} \\ \tau_{xy} & \sigma_y & \tau_{yz} \\ \tau_{xz} & \tau_{yz} & \sigma_z \end{pmatrix}, \quad \sigma' = \begin{pmatrix} \sigma'_x & \tau'_{xy} & \tau'_{xz} \\ \tau'_{xy} & \sigma'_y & \tau'_{yz} \\ \tau'_{xz} & \tau'_{yz} & \sigma'_z \end{pmatrix} \tag{5}$$

$$\sigma' = Q\cdot\sigma\cdot Q^{T}, \quad Q = Q_z .\ Q_y .\ Q_x \tag{6}$$

$$Q_x = \begin{pmatrix} 1 & 0 & 0 \\ 0 & \cos\alpha & \sin\alpha \\ 0 & -\sin\alpha & \cos\alpha \end{pmatrix}, \quad Q_y = \begin{pmatrix} \cos\beta & 0 & -\sin\beta \\ 0 & 1 & 0 \\ \sin\beta & 0 & \cos\beta \end{pmatrix}, \quad Q_z = \begin{pmatrix} \cos\gamma & \sin\gamma & 0 \\ -\sin\gamma & \cos\gamma & 0 \\ 0 & 0 & 1 \end{pmatrix} \tag{7}$$

Where σ is the original stress tensor, σ' is the transformed stress tensor and Q is the transformation matrix. The angles α, β and γ are the Euler angles (see Fig. 8) which are connected to the spatial angles (φ_1, φ_2, φ_3) using:

$$\sin\beta .\ \cos\gamma = \cos\varphi_1, \quad \cos\alpha .\ \sin\beta = -\cos\varphi_2, \quad \beta = \varphi_3 \tag{8}$$

The procedure for calculating the crack angles is as follows: *(i)* A random time step is selected in the solution zone of the finite element model. *(ii)* The stress and strain components in rail elements are calculated for the chosen time step (when the wheel is running over the rail, the stresses can be calculated in the rail elements at any time step). *(iii)* The rail element that experienced the largest equivalent von Mises stress under the wheel passage is determined; the von Mises stress here determines the most critical material point (critical damage location, susceptible to fatigue damage and crack initiation) in the rail. *(iv)* Possible variations with respect to the planar angles are searched and the fatigue parameter is calculated by varying two of these angles (θ_1, θ_2) from zero to 180°; note that $0 \leqslant \theta_1, \theta_2 \leqslant 180$ as shown in Fig. 1(b). *(iv)* The angles, by which the highest fatigue parameter is achieved, are reported as the potential crack angles, while, their corresponding plane is considered as the crack initiation plane.

3.3. Results of numerical simulations

The time histories of stresses and strains of the wheel running over the rail are obtained from the finite element simulations and

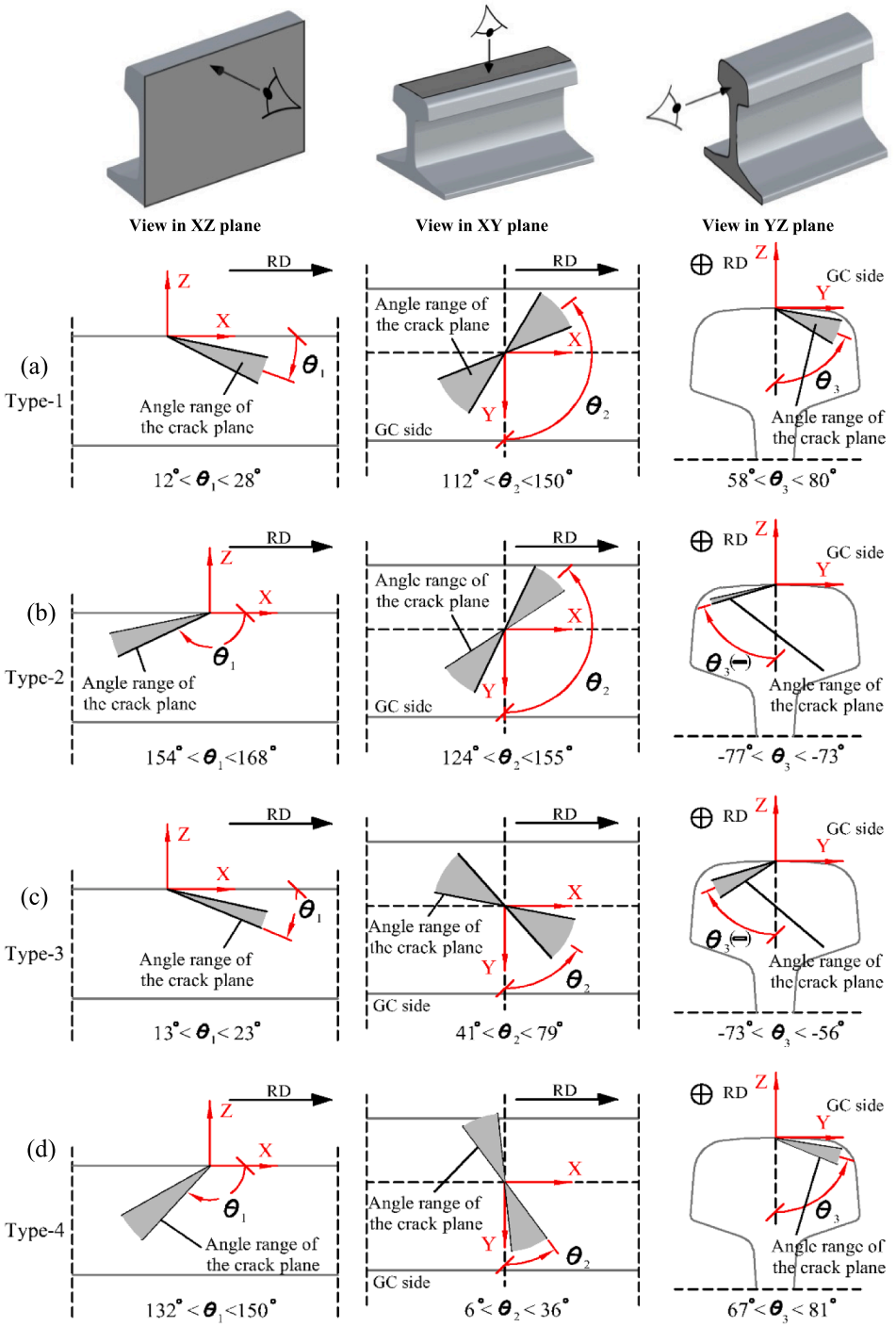

Fig. 12. Ranges of the four crack orientations.

the corresponding fatigue parameters (*FP*) are calculated. Fig. 9 shows the time histories of the V-M stresses experienced by an element in the rail surface during the wheel passage.

The stress components of the rail element when the maximum von Mises stress occur during the wheel passage are calculated (see the given times and peak stress values in Fig. 9). The *FP* parameter is calculated using Eq. (1). For the search of the critical plane, the angles θ_1, θ_2 are varied and the corresponding (transformed) stresses and strains are determined. The values of *FP* with respect to these angles are calculated. Fig. 10 shows the results of the *FP* for the three cases. The dimensionless *FP* values are calculated by

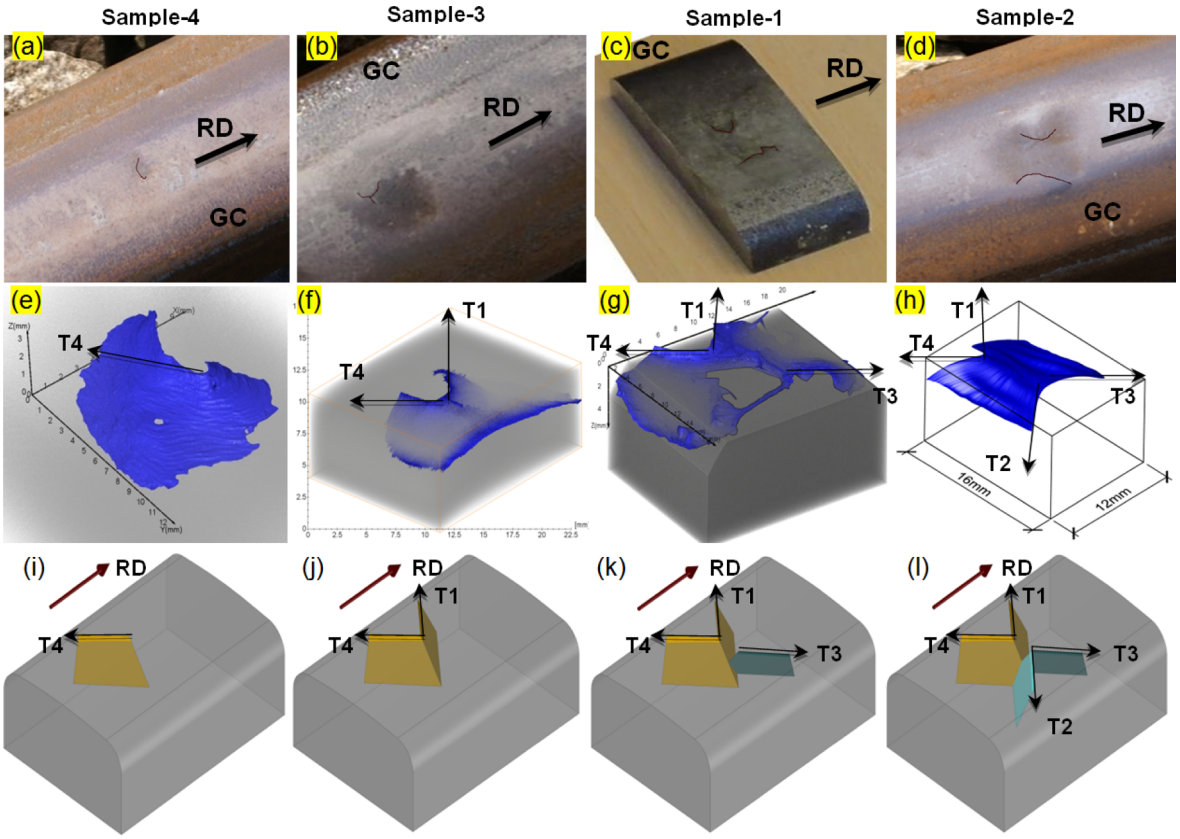

Fig. 13. Four squats (Samples 1–4) with characteristic V-shaped (or U-shaped) peninsula-like crack faces. (a, b, c, d) Top views with the crack mouths highlighted; (e, f, g, h) the reconstructed 3D crack networks; and (i, j, k, l) with increasing crack complexity, the cracks form the characteristic single V-shaped (Sample-3) and double V-shaped (Sample-2) peninsula-like crack faces.

Table 7
Comparison of the variation ranges of θ_1, θ_2, and θ_3 between experiments and FE results. The data are from Tables 4 and 6.

Crack type/angle	T1		T2 μ = −0.35		T3 μ = 0.35		T4 μ = 0	
	Experiments	FEM	Experiments	FEM	Experiments	FEM	Experiments	FEM
θ1	12°–28°	Not seen.	154°–168°	159.9	13°–23°	19.8	132°–150°	158.6
θ2	112°–150°	Not seen.	124°–155°	167.3	41°–79°	17.6	6°–36°	36.9
θ3	58°–80°	Not seen.	73°–77° (–)	−85.3	56°–73° (–)	−83.5	67°–81°	73.6

normalizing the fatigue parameters over the peak value of *FP*; the values of *FP* are indicative and we only search for the angles, by which, the peaks occur.

Based on the *FP* distributions with respect to the angles, the angles of crack initiation are estimated for the element at the centre of the contact area where the pressure is the largest. They are listed in Table 4.

4. Discussion

4.1. Categorization of the crack planes into orientations

The crack planes that intersect the rail surface have been measured and their crack angles distribute over a wide range. In this section, four crack orientations are identified to better categorize and characterize the cracks. These 4 types of orientations, namely, T1 – T4, are illustrated in Fig. 11 in terms of their relative positions and the corresponding angles θ_1, θ_2, and θ_3. The nominal

variation ranges of the angles that correspond to each category are specified at the bottom of this figure. All the crack planes that were measured for the five samples in this research are classified in Table 5 according to the orientation categories.

The proposed crack types (T1-T4) in Fig. 11 are in fact all possible situations, where, a crack plane in the railhead can be located by looking at the defined angle variations in the lower part of Fig. 11.

Table 6 lists the occurrence frequencies of all the crack orientations in the 5 samples. T4 is the most prominent (40%), followed by T1 (30%). T3 and T2 are less frequent with occurrence percentages of 20% and 10%, respectively.

After classifying the crack orientations into the four categories, the variation ranges of the crack angles are calculated; see Table 6. Crack planes C3 in Sample-3 and C6 in Sample-1 are excluded from the results in Table 6, as their corresponding angles deviate substantially from the orientation ranges that were obtained for the other crack planes. Possible explanations for such deviations are that these crack planes are probably not the primary cracks (C3 of Sample-3) or they are due to local disturbances (C6 of Sample-1). The symbol "(–)" in Table 6 indicates that θ_3 is negative for orientations T2 and T3.

The ranges of the orientation angles are plotted in Fig. 12 with the view angles specified on the top. The ranges of T4, which is the most prevalent crack orientation, are plotted in Fig. 12(d).

4.2. Order of crack initiation in multiple cracks

The crack plane is defined as the plane that is tangent to a crack face unit (Section 2.1). Such a definition applies to the cracks in their initiation phase. Because we are not sure which planar face happens earlier in a grown squat, we have studied all the possibilities and calculated all the corresponding angles. The planar faces of the cracks can meet each other and create V-shape or more complex cracks, even in the early stage of crack development. Characterization of such complex cracks seems only possible by discretising them into the planar units as suggested in this study. In this section we discuss the development of cracks.

Squat cracks are reported to initiate from the rail surface; see, e.g., [5] and [13]. The cracks of Sample-5 would support this if they would grow into a squat. The cracks of the other 4 samples are deep and it is not possible to determine their initiation locations from the data that are available. If the 4 orientations, namely, T1 – T4, are ordered according to descending frequency of occurrence as shown in Fig. 13 (i, j, k, l), then T4 and T1, which represent two crack planes, will together form a V-shaped peninsula with a V-shaped crack mouth; see Fig. 13(j) for an idealization and Fig. 13(g) for a real case. In practice, the tip of V may be rounded to become a U, so that the crack mouth appears U-shaped; see Fig. 13(f) for a typical example. Then, T2 and T3 will together form another V-shaped (or U-shaped) peninsula, although much more obtuse. The tips of the two V-shaped peninsulas face each other. Since T4 and T1 have a much higher joint occurrence (70%) than T2 and T3 (30%), it is reasonable to conclude that the peninsula that is formed by T4 and T1 appeared earlier than that by T2 and T3. Thus, the crack that was formed by T4 and T1 is the primary crack and the crack by T2 and T3 the secondary. When a squat develops further in its growth process, the crack network becomes larger and more complex, and additional crack mouths appear in the rail surface. According to these results and Fig. 13, the primary cracks of Sample-1, Sample-3 and Sample-4 are on the gauge side and that of Sample-2 is on the field side. These findings accord with the angle predictions by other researchers, e.g., [8], [11] and [13]. As was concluded from the extensive field monitoring observations of [13], most of the primary cracks started on the gauge side with U-shaped peninsula-like crack faces.

The initiating primary crack in [13] had an angle of approximately 20° with the rail surface; the crack propagated into the rail toward the field side at an angle of approximately 20°; seeα in Fig. 7(c) of [13]. Using the methodology that is proposed in this study, we can approximate such a U-shaped peninsula-like crack face with two main crack orientation planes (T4 and T1). The angle of $\alpha = 20^\circ$ is found to accord with the measured angles of the two crack orientation planes in this study, namely, $\boldsymbol{\theta_1}$ is 12°–28° for T1 and 132°–150° for T4; see Fig. 12.

4.3. Numerical results compared to measured crack angles

In Table 7, the crack angles are compared between the experimental (Table 6) and the FE results (Table 4). Among the four crack types seen from the experimental observations (T1-T4), 3 crack types (T2, T3 and T4) were observed from the FE modelling, for $\mu = -0.35$, 0.35 and 0, respectively; crack type T1 was not seen. This indicates that the crack angles should probably depends on the loading conditions, although the precise loading conditions of the analysed samples are impossible to trace back. According to the results of T2, T3 and T4, it can be seen that the crack angles calculated by the FE modelling are in reasonable agreement with the experiment observation.

The angle ranges θ_1, θ_2, and θ_3 in Table 7 (experimental part) are obtained from the observations on the five squats and cannot be generalized to all squats; however, the other facts mentioned in Discussion support the validity of the results obtained i.e. 1) agreement with the angle predictions by other researchers in the literature and 2) reasonable agreement with the numerical results. The facts mentioned aid in concluding that the crack units of the squat defects appear to form within the ranges indicated in this study.

5. Conclusions

By defining crack planes, this study measured the angles of squat cracks that intersected the rail surface and identified the

characteristic orientations of the cracks. CT scanning and metallographic observations were used to reconstruct the complex geometries of crack networks in squats of various severities. Finite element modelling is employed to relate the stress state to the crack angles. The following conclusions were drawn:

(1) Using the proposed 3D visualization method, including the definitions of crack planes and angles, we were able to define and measure the 3D geometries of squats with complex crack networks. The method was successfully applied to squat defects of various severities.
(2) Four crack orientations, namely, T1-T4, were identified and visually demonstrated.
(3) The ranges of the characteristic crack angles of the four orientations were measured for 5 samples. The cracks have an angle of 132°-150° relative to the *X*-axis (θ_1). The angle in the rail surface relative to the *Y*-axis (θ_2) was in the range of 6°-36°. In the rail vertical-longitudinal cross-section, the angle of the crack relative to the *Z*-axis (θ_3) was in the range of 67°-81°. These findings accorded with angle predictions by other researchers, e.g., [8,11], and with the field monitoring research of [13].
(4) The occurrence frequencies of the orientations were calculated for the samples, based on which it was found that orientations T4 and T1 together form a V-shaped (or U-shaped) peninsula, which is the primary crack of squats and accords with the findings in the literature [13]. T2 and T3 together form V-shaped secondary cracks.
(5) The crack angles calculated by the FE modeling were in agreement with the experimental observations. The angle types T2, T3 and T4 seem to correspond to braking, traction and free rolling loading, respectively. This indicates that the crack initiation angle depends on the loading conditions. Further investigation on this is needed.

Declaration of Competing Interest

The authors declare that they have no known competing financial interests or personal relationships that could have appeared to influence the work reported in this paper.

Acknowledgements

This research is part of an ExploRail project, namely, Development of High–Performance Rail through Intelligent Metallurgy and Engineering (PRIME), which was conducted at Delft University of Technology. This project (Code: 11247) is funded by Dutch rail infra manager ProRail and the Netherlands organization for scientific research (STW/NWO).

Appendix A. The 3D geometry of the internal cracks and measuring the crack angles in all the rail samples

See Figs. 14–18.

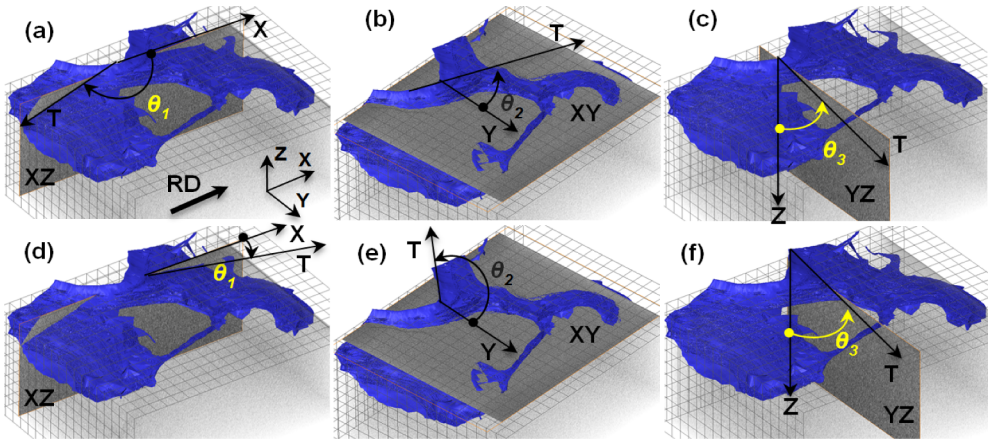

Fig. 14. Measuring the crack angles of the crack planes in Sample-1. (a, b, c) the angles for C1 and (d, e, f) the angles for C2. Arrow T represents the average tangent line to the crack segments in the rail surface. The angles that are associated with C1 and C2 are shown here as examples.

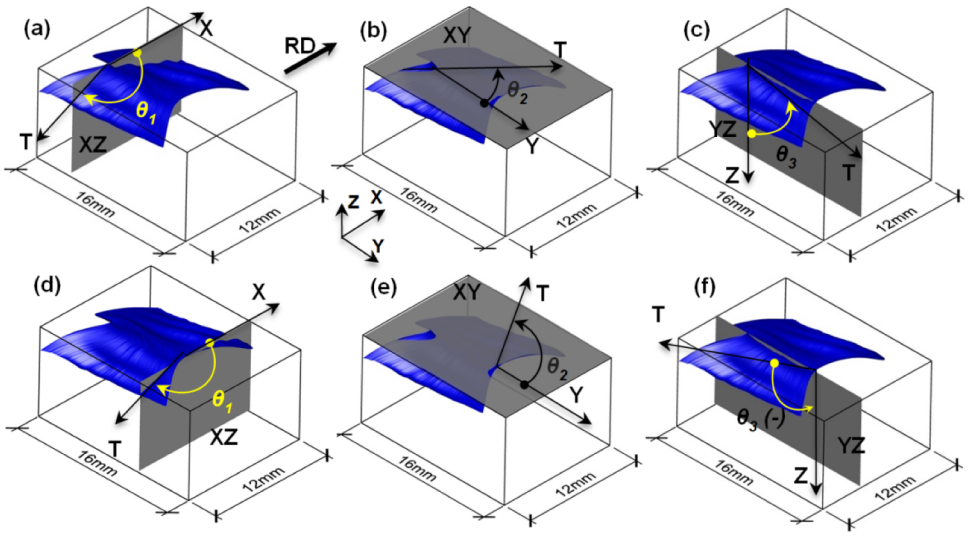

Fig. 15. Measuring the crack angles in Sample-2. (a, b, c) The angles that are associated with C3 and (d, e, f) the angles that are associated with C1; the crack angles that are associated with C3 and C1 are shown here as examples.

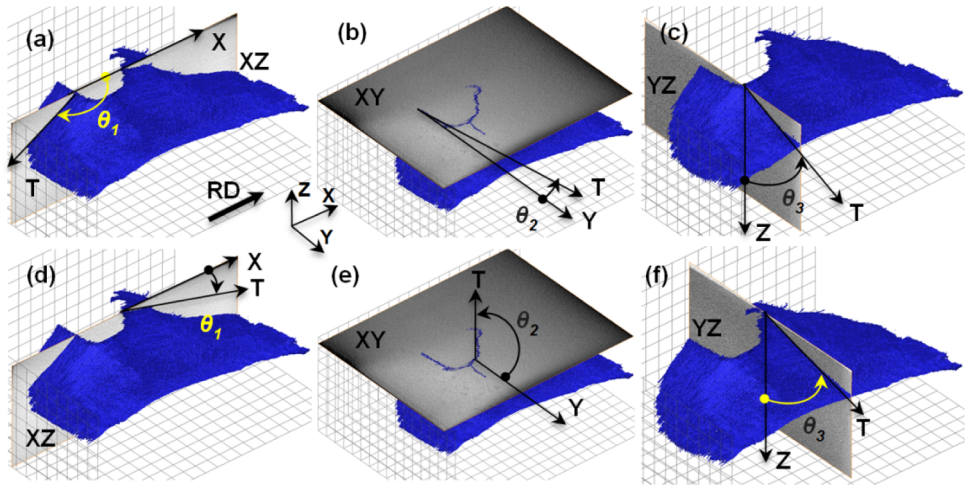

Fig. 16. Measuring the angles of the crack planes that intersect the rail surface in Sample-3; (a, b, c) the angles for C4 and (d, e, f) the angles for C5; the results for C4 and C5 are presented as examples.

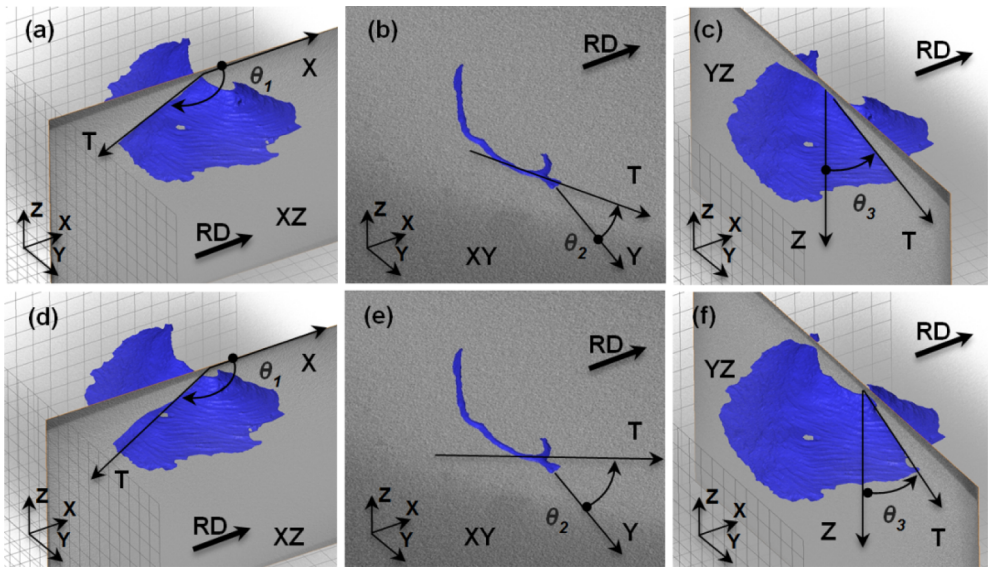

Fig. 17. Measuring the angles for the crack planes in Sample-4; (a, b, c) the angles for C1 and (d, e, f) the angles for C2.

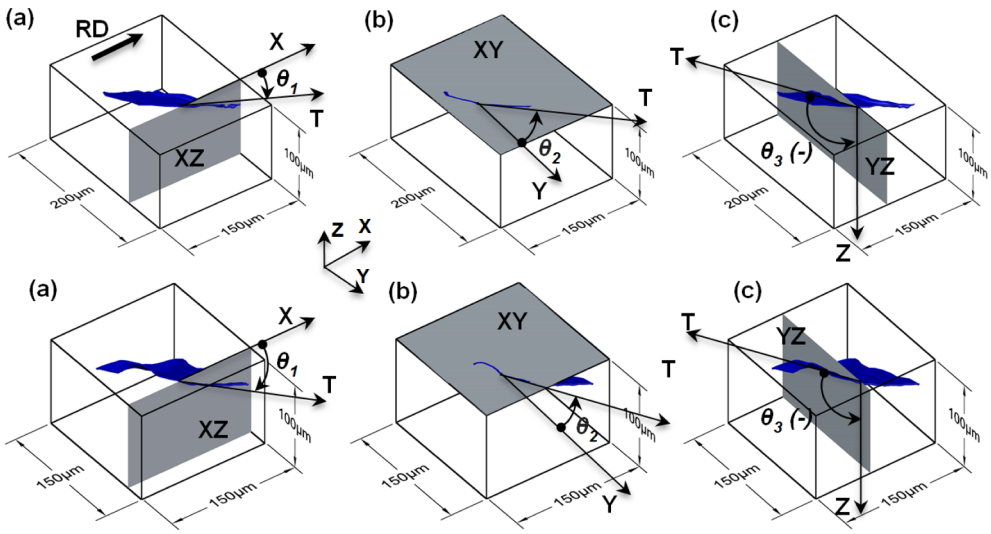

Fig. 18. Measuring the crack angles for the two tiny cracks in Sample-5; (a, b, c) The angles for C1 and (d, e, f) the angles for C2.

References

[1] Li Z, Zhao X, Esveld C, Dollevoet R, Molodova M. An investigation into the causes of squats—correlation analysis and numerical modeling. Wear 2008;265:1349–55.
[2] Bogdanski S, Olzak M, Stupnicki J. Numerical modelling of a 3D rail RCF 'squat'-type crack under operating load. Fatigue & Fracture Eng Mater Struct 1998;21:923–35.
[3] Farjoo M, Daniel W, Meehan PA. Modelling a squat form crack on a rail laid on an elastic foundation. Engng Fract Mech 2012;85:47–58.
[4] Bogdanski S, Olzak M, Stupnicki J. Numerical stress analysis of rail rolling contact fatigue cracks. Wear 1996;191:14–24.
[5] Pal S, Daniel WJT, Farjoo M. Early stages of rail squat formation and the role of a white etching layer. Int J Fatigue 2013;52:144–56.
[6] Simon S, Saulot A, Dayot C, Quost X, Berthier Y. Tribological characterization of rail squat defects. Wear 2013;297:926–42.
[7] Naeimi M, Li S, Li Z, Wu J, Petrov RH, Sietsma J, et al. Thermomechanical analysis of the wheel-rail contact using a coupled modelling procedure. Tribol Int 2018;117:250–60.
[8] Ringsberg J, Loo-Morrey M, Josefson B, Kapoor A, Beynon JH. Prediction of fatigue crack initiation for rolling contact fatigue. Int J Fatigue 2000;22:205–15.
[9] Deng X, Li Z, Qian Z, Zhai W, Xiao Q, Dollevoet R. Pre-cracking development of weld-induced squats due to plastic deformation: five-year field monitoring and numerical analysis. Int J Fatigue 2019;127:431–44.
[10] Franklin F, Kapoor A. Modelling wear and crack initiation in rails. Proc Inst Mech Eng, Part F: J Rail Rapid Transit 2007;221:23–33.
[11] Akama M, Matsuda H, Doi H, Tsujie M. Fatigue crack initiation life prediction of rails using theory of critical distance and critical plane approach. J Comput Sci Technol 2012;6:54–69.
[12] Ringsberg J, Josefson B. Finite element analyses of rolling contact fatigue crack initiation in railheads. Proc Inst Mech Eng, Part F: J Rail Rapid Transit

2001;215:243–59.
[13] Deng X, Qian Z, Li Z, Dollevoet R. Investigation of the formation of corrugation-induced rail squats based on extensive field monitoring. Int J Fatigue 2018;112:94–105.
[14] Li S, Wu J, Petrov RH, Li Z, Dollevoet R, Sietsma J. "Brown etching layer": A possible new insight into the crack initiation of rolling contact fatigue in rail steels? Engng Fail Anal 2016;66:8–18.
[15] Deng X, Qian Z, Dollevoet R. Lagrangian explicit finite element modeling for spin-rolling contact. J Tribol 2015;137:041401.
[16] Naeimi M, Li Z, Qian Z, Zhou Y, Wu J, Petrov RH, et al. Reconstruction of the rolling contact fatigue cracks in rails using X-ray computed tomography. NDT and E Int 2017;92:199–212.
[17] Garnham JE, Fletcher DI, Davis CL, Franklin FJ. Visualization and modelling to understand rail rolling contact fatigue cracks in three dimensions. Proc Inst Mech Eng, Part F: J Rail Rapid Transit 2011;225:165–78.
[18] Yang Z, Deng X, Li ZZ. Numerical modeling of dynamic frictional rolling contact with an explicit finite element method. Tribol Int 2019;129:214–31.
[19] Das J, Sivakumar S. An evaluation of multiaxial fatigue life assessment methods for engineering components. Int J Press Vessels Pip 1999;76:741–6.
[20] You BR, Lee SB. A critical review on multiaxial fatigue assessments of metals. Int J Fatigue 1996;18:235–44.
[21] Ringsberg JW. Life prediction of rolling contact fatigue crack initiation. Int J Fatigue 2001;23:575–86.
[22] Zoeteman A, Dollevoet R, Li Z. Dutch research results on wheel/rail interface management: 2001–2013 and beyond. Proc Inst Mech Eng, Part F: J Rail Rapid Transit 2014;228(6):642–51.
[23] Jiang Y, Sehitoglu H. A model for rolling contact failure. Wear 1999;224:38–49.
[24] Akama M. Development of finite element model for analysis of rolling contact fatigue cracks in wheel/rail systems. Railway Technical Research Institute, Quarterly Reports, 48; 2007.